

# Functional imaging of small tissue volumes with diffuse optical tomography

Alexander D. Klose\* and Andreas H. Hielscher†

Departments of Biomedical Engineering & Radiology

Columbia University, 500W 120th Street, ET351 Mudd Bldg., New York, NY 10027, USA

## ABSTRACT

Imaging of dynamic changes in blood parameters, functional brain imaging, and tumor imaging are the most advanced application areas of diffuse optical tomography (DOT). When dealing with the image reconstruction problem one is faced with the fact that near-infrared photons, unlike X-rays, are highly scattered when they traverse biological tissue. Image reconstruction schemes are required that model the light propagation inside biological tissue and predict measurements on the tissue surface. By iteratively changing the tissue-parameters until the predictions agree with the real measurements, a spatial distribution of optical properties inside the tissue is found. The optical properties can be related to the tissue oxygenation, inflammation, or to the fluorophore concentration of a biochemical marker. If the model of light propagation is inaccurate, the reconstruction process will lead to an inaccurate result as well. Here, we focus on difficulties that are encountered when DOT is employed for functional imaging of small tissue volumes, for example, in cancer studies involving small animals, or human finger joints for early diagnosis of rheumatoid arthritis. Most of the currently employed image reconstruction methods rely on the diffusion theory that is an approximation to the equation of radiative transfer. But, in the cases of small tissue volumes and tissues that contain low scattering regions diffusion theory has been shown to be of limited applicability. Therefore, we employ a light propagation model that is based on the equation of radiative transfer, which promises to overcome the limitations.

**Keywords:** functional imaging, diffuse optical tomography, small animal imaging, equation of radiative transfer, finger joint imaging, fluorescence tomography, tissue optics

## 1. INTRODUCTION

Over the last decade considerable advances have been made toward tomographic imaging of biological tissue using near-infrared light in the wavelength range of 600 nm to 900 nm.<sup>1</sup> The light propagation in biological tissue is governed by the spatial distribution of optical properties such as the scattering,  $\mu_s$ , and absorption,  $\mu_a$ , coefficients. Since biological tissue is highly scattering, direct imaging of interior tissue parts, contrast agents, or physiological processes is almost impossible. Diffuse optical tomography (DOT) is an imaging modality that provides the spatial distribution of optical properties when probing the tissue with laser light and measuring the light distribution on the tissue surface. A reconstructed three-dimensional (3D) spatial map of optical properties or contrast agent concentration supplies valuable clinical information. A comprehensive review about DOT has been given Gibson et al.<sup>2</sup>

Besides versatile instrumentation DOT requires novel image reconstruction algorithms that typically consist of two parts: (1) a forward model for light propagation and (2) an inverse model. The forward model predicts the detector readings on the tissue boundary given a distribution of optical properties inside the medium. On the other hand, the inverse model determines the optical parameters inside the tissue, given a set of detector readings and detector predictions on the boundary of the tissue. The forward and inverse models are iteratively employed within an optimization method. The predicted detector readings of the forward model on the tissue surface are subsequently compared to measured detector readings by defining an objective function, e.g.  $\chi^2$ -error norm. The objective function is minimized within an optimization method for non-linear functions, such as conjugate gradient or quasi-Newton methods. The optical parameters at the minimum are considered as the solution of the inverse problem.<sup>3,4</sup>

\* Email: [ak2083@columbia.edu](mailto:ak2083@columbia.edu), Phone: 212-854 5868

† Email: [ahh2004@columbia.edu](mailto:ahh2004@columbia.edu), Phone: 212-8545080

The light propagation in tissue is governed by the equation of radiative transfer (ERT) for diffuse and non-diffusive regimes. The ERT needs to be solved with numerical methods since no analytical solutions of the ERT exist for non-uniform media with complex geometries. These numerical methods are low-order approximations to the ERT, such as the diffusion approximation, or high-order approximations to the ERT, e.g. discrete ordinates methods. The spatial discretization of the tissue domain can either be performed with finite-difference, finite-volume, or finite-element techniques. The diffusion approximation is most commonly employed for DOT and has been successful for imaging of tissue with large geometries and tissue with diffusive regimes where  $\mu_s \gg \mu_a$ , e.g. imaging of the female breast or imaging of muscular tissue. However, the diffusion approximation has limited applications when applied to tissue with small geometries, tissue with high absorption, or tissue containing void-like areas.<sup>5</sup> In that case, high-order approximations of the ERT are required such as discrete-ordinates methods.

We will give an overview about functional imaging using DOT, and we will show three examples that employ the ERT as part of an image reconstruction method for recovering the optical properties. First, we demonstrate the reconstruction of optical properties in human finger joints for early diagnosis of rheumatoid arthritis. Reconstructing the spatial map of scattering and absorption coefficients provides valuable clinical information about the healthy or inflamed stage of finger joints. Furthermore, the joint cavity contains a low scattering fluid that constitutes a non-diffusive regime for near-infrared light. Hence, the small finger geometry and the void-like joint cavity require an ERT-based image reconstruction method.

Another application of ERT-based image reconstruction algorithms is small animal imaging. Small animals are increasingly used as model for human disease in biomedical research. In particular, we studied the growth and regression of Wilms tumors implanted in the kidneys of NCR athymic nude mice to judge the efficacy of an anti-vascular endothelial growth factor (VEGF) treatment. VEGF is a polypeptide that is secreted by cells and acts as a mitogen for vascular endothelial cells and stimulates the formation of new blood vessels, a process called angiogenesis. Effective anti-VEGF therapies block the action of VEGF and prevent the growth of new blood vessels in the tumor. It has been shown in several animal studies that disruption of VEGF signaling can attenuate or even abolish tumor vasculature, producing marked tumor regression.

Furthermore, we started to apply ERT-based algorithm to the problem of fluorescence molecular tomography (FMT). In FMT biochemical fluorescent markers are injected into cancer-bearing rodents, and upon excitation with an external light source the fluorescent marker will emit light. The fluorescent light is detected with a CCD camera on the tissue surface. Subsequently, a spatial map of the fluorescent marker concentration is reconstructed that, e.g., allows to monitor the growth of a tumor or the effectiveness of new anti-cancer drugs.

## 2. RADIATIVE TRANSFER MODEL

Most light propagation models in DOT are based on the diffusion equation, which is a low-order approximation to the ERT. However, the diffusion approximation has limited applicability in highly absorbing media, media with low-scattering regions, and media with small geometries where boundary effects are dominating. We use a discrete-ordinates formulation of the ERT that can be applied to tissues with small geometries or tissues containing void-like areas. Our ERT-based light propagation model takes the refractive index mismatch at the tissue-air boundary into account.

The ERT in biological tissue is a balance equation for the angular flux  $\Psi(r, \Omega)$  of photons and is given by

$$\Omega \cdot \nabla \Psi(r, \Omega) + (\mu_a + \mu_s) \Psi(r, \Omega) = \mu_s \int_{4\pi} p(\Omega, \Omega') \Psi(r, \Omega') d\Omega' . \quad (1)$$

The boundary condition with light sources  $S$  for all directions  $\Omega \cdot n < 0$  with  $n$  being normal outward vector is given by

$$\Psi(r, \Omega) = S(r, \Omega) + R(\Omega \cdot n) \Psi(r, \Omega') . \quad (2)$$

The fundamental quantity in the ERT is the radiance  $\Psi(r, \Omega)$  at the spatial position  $r$  and unit direction  $\Omega$ . Other quantities besides the radiance  $\Psi(r, \Omega)$  that are included in the ERT are the scattering coefficient,  $\mu_s$ , the absorption coefficient,  $\mu_a$ , and the scattering phase function  $p$ . The physical quantity  $R$  constitutes the reflectivity at the air-tissue boundary due to the refractive index mismatch.

The ERT, as given by equation (1), is used for transillumination imaging, where laser sources are placed on the tissue boundary. In the case of fluorescence imaging of fluorophores, a second ERT [equation (3)] is needed that describes the propagation of fluorescent light after the fluorophores have been excited with an external light source.<sup>6,7</sup>

$$\Omega \cdot \nabla \Psi(r, \Omega) + (\mu_a + \mu_s) \Psi(r, \Omega) = \frac{1}{4\pi} \eta \mu_a^{\beta} \int_{4\pi} \Psi^x d\Omega + \mu_s \int_{4\pi} p(\Omega, \Omega') \Psi(r, \Omega') d\Omega' \quad (3)$$

The radiance  $\Psi^x$  is calculated with the first ERT as given by equation (1). The fluorophore absorption is given by  $\mu_a^{\beta}$ . The ERT is solved numerically with a finite-difference discrete-ordinates (S<sub>N</sub>) method.<sup>8,9,10</sup> The irregular geometry of the mouse surface is taken into account with a blocking-off region method. More details about modeling the fluorescent system are given by Klose et al.<sup>7</sup>

### 3. IMAGE RECONSTRUCTION

The spatial distributions of optical parameters, the scattering coefficient  $\mu_s$ , the absorption coefficient  $\mu_a$ , or the fluorophore absorption  $\mu_a^{\beta}$ , are reconstructed by applying nonlinear optimization techniques to an objective function  $\Phi$ , which describes the difference between the measured  $M_d$  and predicted data  $P_d$  for all D source-detector pairs

$$\Phi(\mu_a^{x \rightarrow m}) = \sum_d (M_d - P_d(\mu_a^{x \rightarrow m}))^2 / \sigma_d^2 \quad (4)$$

The predicted data  $P_d$  are calculated by equations (1) or (3), whereas  $M_d$  is given by an experiment. We minimize the objective function (4) by using gradient-based optimization techniques. Gradient-based optimization techniques have been proven to be computationally efficient for large-scale problems such as in OT, where between  $10^3$  and  $10^5$  unknown optical parameters are common. These optimization techniques use the gradient  $\nabla \Phi$  of the objective function with respect to the optical parameters  $\mu_s$  and  $\mu_a$  for calculating a search direction  $u_k$  to find a new update  $\mu_{k+1}$  of optical parameters. An updating scheme determines, for example, a new estimate of the sequence  $\mu_k$  of optical parameters:

$$\mu_{k+1} = \mu_k + \alpha u_k \quad (3)$$

Therefore, calculating the new estimate  $\mu_{k+1}$  is broken up into two tasks: (1) finding a proper step length  $\alpha$  and (2) calculating the search direction  $u_k$ .<sup>11</sup> Gradient techniques differ mainly in the way the step length  $\alpha$  and the search direction  $u_k$  are calculated. In DOT, the most common method to determine the search direction has been the nonlinear conjugate gradient (CG) technique. However, we use the more complex quasi-Newton (QN) method that provides better reconstruction results. Once the minimum is found, the final result is the spatial distribution of the optical parameters.

## 4. EXAMPLES

### 4.1 Imaging of Finger Joints for Diagnosis of Early Rheumatoid Arthritis

Rheumatoid Arthritis (RA) is one of the most common diseases of human joints of the hands and feet. RA is a progressive disease and is characterized by an inflammation process that originates in the inner membrane (*synovial membrane* or *synovium*) of the joint capsule and spreads to other parts of the joint. Routine imaging techniques for

early diagnosis do not exist. However, first clinical results of optical techniques show that DOT might facilitate the diagnosis of early stages of RA.<sup>12,13</sup> Information about the optical properties of the synovium, obtained from DOT, could be used to distinguish between healthy and early stages of rheumatoid conditions. Since we have void like areas (scattering coefficient of synovial fluid is smaller than  $0.1 \text{ cm}^{-1}$ ) inside the finger joint, ERT-based reconstruction methods are required.

Figure 1a) shows a sagittal cross-section of a human finger joint. The region of interest (ROI), enclosed by the red line, constitutes a proximal interphalangeal (PIP) joint. The synovial fluid inside the joint cavity between the two bones is low-scattering, but increased scattering can be found when RA is present.

A laser diode illuminated the interior side of the ROI of the joint at 11 different positions with light at wavelength  $\lambda = 678 \text{ nm}$ . A single detector measured the transmitted light on the posterior side of the joint at 16 different positions. The scattering coefficients  $\mu_s$  of the ROI were reconstructed with our ERT-based image reconstruction method to obtain sagittal images of the finger joint. The Cartesian finite-difference mesh covered a cross-sectional area of  $4 \text{ cm} \times 2.1 \text{ cm}$  of the finger joint. We considered anisotropic scattering and Fresnel boundary conditions with a refractive index of  $n=1.5$ . The reconstructed image of  $\mu_s$  of a healthy finger joint is shown in Figure 1b). The top of the image depicts the interior side and the bottom of the image constitutes the posterior side of the finger. Small scattering coefficients can be found in the joint cavity, which indicates a healthy finger joint with an optically clear synovial fluid. However, the reconstructed optical parameters are not as small as the real optical parameters of the synovial fluid within the joint cavity due to the limited spatial resolution of optical reconstruction techniques. Thus, the area of the cavity in the image, which is covered by the decrease of optical parameters, is larger than the real joint cavity. The adjacent tissue parts to the left and to the right in the image depict the bones. Figure 1c) shows the reconstructed scattering coefficient distribution of a finger joint with rheumatoid arthritis. The scattering coefficient is significantly elevated inside the joint cavity.

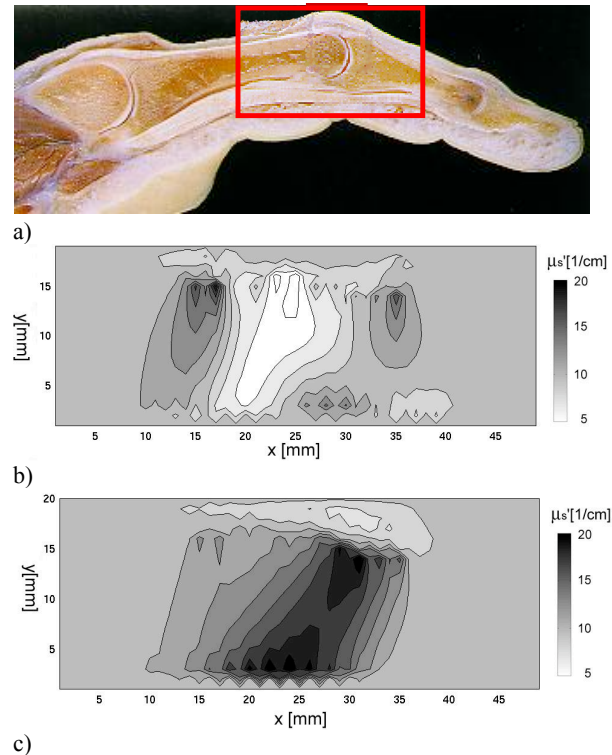


Figure 1: a) Cross-sectional cut (sagittal view) of human finger joint with ROI enclosed by red line. The reconstructed scattering coefficients of the ROI are shown in b) for a healthy finger joint, and in c) for a joint with rheumatoid arthritis.

## 4.2. Imaging of Tumor Growth and Regression

We studied the efficacy of an anti-vascular endothelial growth factor (VEGF) treatment of Wilms tumors implanted in the kidneys of NCR athymic nude mice. VEGF stimulates the formation of new blood vessels, a process called angiogenesis. Effective anti-VEGF therapies block the action of VEGF and prevent the growth of new blood vessels in the tumor. They can even destabilize the newly formed blood vessels and cause tumor regression. It has been shown in several animal studies that disruption of VEGF signaling can attenuate or even abolish tumor vasculature, producing marked tumor regression. More details of our study can be found in Masciotti et al.<sup>14,15</sup>

In our study, tumors cells were injected into the left kidney of a nude mouse and allowed to grow undisturbed for 30 days. In order to judge the potential for monitoring tumor growth in the mouse tumor model, the mouse was imaged every 7 days with MRI and twice every seven days with DOT for a length of 22 days. On the 52<sup>nd</sup> day after implantation, a treatment schedule consisting of two injections a week was begun.

The mouse was imaged with our optical imaging system consisting of an imaging chamber (cylindrical container) with optical fibers attached. The cylinder made from white Delrin had a diameter of 5 cm and a height of 10 cm. Two fiber-holding rings machined from black Delrin had 24 holes drilled, angularly spaced 15° apart, allowing 12 source and 12 detector fiber bundles to be connected to each ring in an alternating pattern. The tumor-bearing mouse was positioned inside the Delrin cylinder, which also contained a 1% Intralipid matching fluid in order to reduce edge effects during reconstructions and to ensure that the propagation of light into the tissue can be correctly modeled by our reconstruction algorithm. Laser light at two wavelengths (wavelengths  $\lambda_1 = 760$  and  $\lambda_2 = 830$  nm) was delivered to the source fiber bundles via an optical demultiplexing switch, which allows light to be sequentially delivered to different positions.

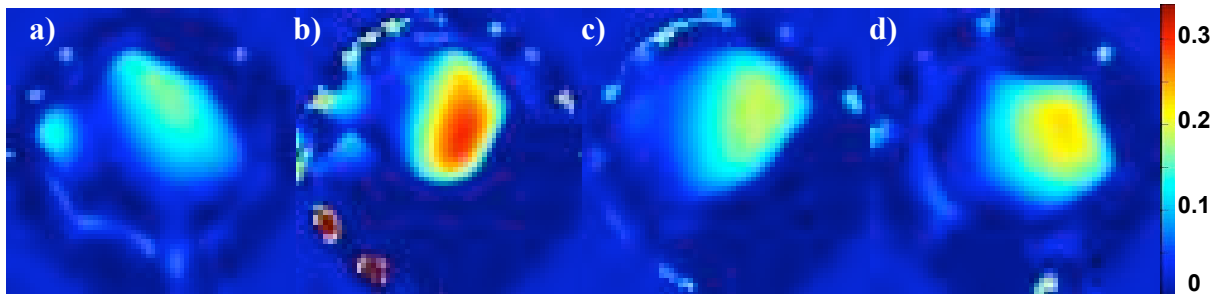


Figure 2: Optical tomographic images of the absorption coefficient  $\mu_a$  ( $\text{cm}^{-1}$ ) of a tumor-bearing mouse on the a) 49<sup>th</sup>, b) 52<sup>nd</sup>, c) 53<sup>rd</sup>, and d) 54<sup>th</sup> day. a) and b) show images on the days before treatment, whereas c) and d) show images after treatment.

Two types of scans, one static and one dynamic, were performed. For static imaging the mouse was secured in the probe for just under 3 minutes while the tomographic data sets were acquired. For dynamic imaging, a syringe was stabilized on a surface so that the treatment injection could be administered through the cannula with causing minimal movement inside the probe. The optical scan was performed continuously for approximately 50 minutes.

In this study we show two-dimensional (2D) reconstructed axial absorption coefficient maps that we suggest are proportional to the blood volume in the tumor. Figure 2 shows static optical tomographic images of the mouse with the kidney tumor. The image series depicts the tumor on the a) 49<sup>th</sup>, b) 52<sup>nd</sup>, c) 53<sup>rd</sup>, and d) 54<sup>th</sup> day after implantation. In all cases, the area of absorption is in the same area of the mouse, that the MRI images show the tumor to be located. There is a larger absorption coefficient on the 52<sup>nd</sup> day compared to the 49<sup>th</sup> day. We believe this is due to an increase in tumor blood volume due to general increase in tumor size. This drastic increase in tumor size can also be seen in the MRI images. The tumor was treated after the scan on the 52<sup>nd</sup> day. There is lower absorption on the 53<sup>rd</sup> day

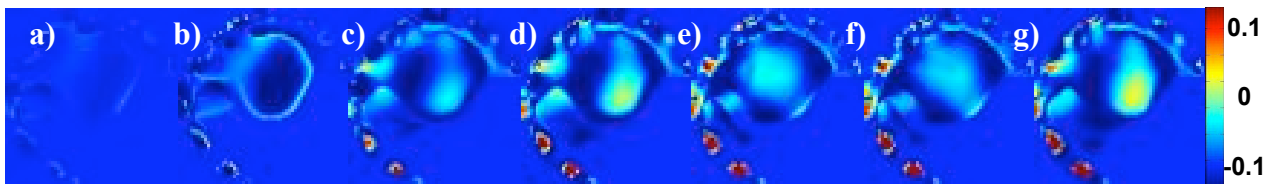


Figure 3: Maps of changes in the absorption coefficient  $-\Delta\mu_a$  ( $\text{cm}^{-1}$ ) with respect to figure 2b) for a) 0, b) 4, c) 8, d) 16, e) 20, f) 24, and g) 32 minutes after injection.

compared to the 52<sup>nd</sup> day which we believe is due to a decrease in blood volume in the tumor as a result of drug-induced blood vessel destruction.

Dynamic optical tomographic images were also taken on the 52<sup>nd</sup> day after implantation. The treatment was administered 4 minutes into the scan at time 0. The large circular shape corresponds to the cylinder cross-section. Small areas of high absorption on the edge of the circle are source-boundary artifacts. The mouse was located with back against the rear of the cylinder (top of image). The area of high absorption is collocated with the tumor as confirmed with MRI. Figures 3a) to 3g) show images that represent the difference of the original absorption image

[Figure 2b)] and the absorption image at each of the various time points. At 8 minutes after drug injection [Figures 3c)] one can observe a decrease in absorption around the periphery of the tumor and an increase in absorption inside the tumor. A decrease in the absorption coefficient inside the tumor occurs thereafter. By 32 minutes after injection a large decrease in absorption coefficient is observed inside the tumor. In most cases we observed that this or an even stronger decrease is still present 24 hours after treatment.

### 4.3. Imaging of Fluorescent Sources in Small Animals

Optical molecular imaging has emerged in recent years, which uses near-infrared fluorescent probes.<sup>16</sup> A fluorescent biochemical marker is injected into a small animal such as mice and will emit near-infrared light upon excitation by an external light source. From measurements of the light intensity on the tissue surface one seeks to determine the spatial concentration distribution of the marker inside the tissue. Since the fluorescent light signal is proportional to the fluorophore uptake in tissue, the molecular probe concentration can be derived.

We have recently presented the first transport-theory-based, three-dimensional, tomographic reconstruction algorithm for fluorescence molecular tomography (FMT).<sup>6</sup> The ERT-based model is particularly well-suited to take small geometries and small source-detector separations into account as they are encountered in FMT of small animals. We have tested the performance of the code with an in vivo mouse model for Lewis Lung Carcinoma (LLC).<sup>17,18</sup> The animal was injected with a Cy5.5-based fluorescent probe (quantum yield 0.28 and extinction 250,000 M cm<sup>-1</sup>) with high sensitivity to cathepsins.

Cathepsins are lysosomal enzymes for protein degradation, which can also be present in the extracellular space of cancerous cells. Fluorescent molecular probes are exposed to these cathepsins inside the extracellular matrix and are subsequently activated and emit fluorescent light. For the data acquisition the mouse was immersed into an imaging chamber containing a scattering matching fluid. The imaging chamber had a size of 4×4×1.3 cm<sup>3</sup>. One side of the chamber was illuminated with light ( $\lambda = 674nm$ ) emerging from 46 fibers arranged in a symmetric pattern [crosses in Figure 4a)]. A CCD camera captured the excitation and fluorescence light ( $\lambda = 694nm$ ) on the side opposite to the illuminating fibers [circles in Figure 4a)]. Figure 4a) shows a surface-weighted fluorescence image of the mouse model with a LLC on the left side, but no spatial information of the fluorophore concentration is available. Figures 4b) to 4f) show tomographic images of the fluorophore concentration at different depths.

## 5. SUMMARY

We have developed image reconstruction algorithms for diffuse optical tomography (DOT) that recover the spatial distribution of optical properties in small tissue volumes. In this case it is necessary to model light propagation with the equation of radiative transfer rather than with the diffusion approximation. The reconstructed images of the absorption coefficient, scattering coefficient, or fluorescent probe concentration can be used, for example, for functional imaging of tumor growth and regression in small animal models, detecting early rheumatoid arthritis in human finger joints, and

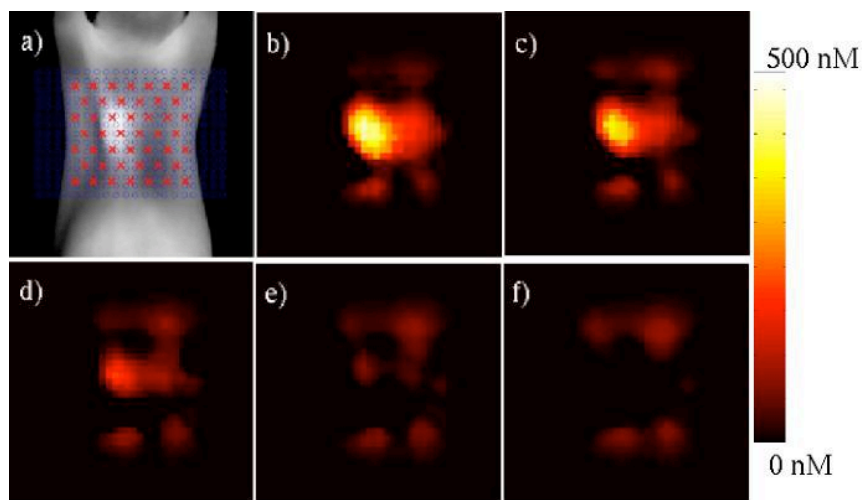


Figure 4: Image reconstruction of fluorophore concentration of a cancer bearing mouse (Lewis Lung Carcinoma). Images b) to f) are given for different depths  $d$  from the top plane (detector plane). Figure a) shows the source-detector configuration, where the red crosses identify source locations and the light blue square identifies the CCD detection area. Different depths: b) 0.1 cm c) 0.3cm, d) 0.5 cm, e) 0.7 cm, and f) 0.9 cm.

for functional imaging of tumor models on a molecular and cellular level. In particular, DOT can be used for monitoring the change of the scattering coefficient in human PIP joints for early diagnosis of RA. Large scattering coefficients can be found inside the joint cavity when RA is present, whereas small scattering coefficients are present in healthy PIP joints. Furthermore, we have employed DOT for monitoring the physiological changes that follow the administration of an anti-VEGF treatment in tumor-bearing mice. We observed an effect as early as eight minutes after administration of the drug. We found a decrease in absorption, which we believe corresponds to a decrease in tumor blood volume. This drop in blood volume is most likely due to the fact that blocking VEGF causes a decrease in nitric oxide, which in turn leads to vascular constriction. Last, we have shown results concerning fluorescence tomographic imaging of molecular probe concentrations in tumor models in small animals.

## 6. ACKNOWLEDGEMENTS

This work was supported in part by the National Institute of Arthritis and Musculoskeletal and Skin Diseases (NIAMS - grant 2R01 AR46255-04), the National Institute of Biomedical Imaging and Bioengineering (NIBIB - grant 5R01-EB001900), the National Cancer Institute (NCI-grant 5R33-CA91807, Hielscher; NCI-grant 5R01CA100451, Kandel), and the Ernst-Schering Research Foundation. The authors would like to thank Dr. Kandel (Dept. of Surgery, Columbia University New York), James Masciotti (Dept. of Biomedical Engineering, Columbia University New York), Dr. Ntziachristos (MGH, Harvard Medical School, Charlestown), Dr. Scheel (Dept. of Medicine, University of Gottingen, Germany), Dr. Beuthan (Dept. of Medical Physics, Charite Berlin, Germany) for their valuable input and contributions.

## REFERENCES

- <sup>1</sup> A.H. Hielscher, A.Y. Bluestone, G.S. Abdoulaev, A.D. Klose, J. Lasker, M. Stewart, U. Netz, J. Beuthan, "Near-infrared diffuse optical tomography," *Disease Markers* **18(5-6)**, pp. 313-337 (2002).
- A.P. Gibson, J.C. Hebden, S.R. Arridge, "Recent advances in diffuse optical imaging," *Phys. Med. Biol.* **50(4)**, pp. R01-R43 (2005).
- A.H. Hielscher, A.D. Klose, and K.M. Hanson, "Gradient-based iterative image reconstruction scheme for time-resolved optical tomography," *IEEE Trans. Med. Imag.* **18(3)**, pp. 262-271 (1999).
- A.D. Klose and A.H. Hielscher, "Iterative reconstruction scheme for optical tomography based on the equation of radiative transfer," *Med. Phys.* **26(8)**, pp. 1698-1707 (1999).
- A.H. Hielscher, R.E. Alcouffe, and R.L. Barbour, "Comparison of finite-difference transport and diffusion calculations for photon migration in homogeneous and heterogeneous tissues," *Phys. Med. Biol.* **43**, pp. 1285-1302 (1998).
- A.D. Klose and A.H. Hielscher, "Fluorescence tomography with simulated data based on the equation of radiative transfer," *Opt. Lett.* **28(12)**, pp. 1019-1021 (2003).
- A.D. Klose, V. Ntziachristos, A.H. Hielscher, "The inverse source problem based on the radiative transfer equation in optical molecular imaging," *Journal of Computational Physics* **202**, pp. 323-345 (2005).
- K.M. Case, P.F. Zweifel, *Linear Transport Theory*, Addison-Wesley, Massachusetts, 1967.
- E.E. Lewis and W.F. Miller. *Computational Methods of Neutron Transport*, John Wiley & Sons, New York, 1984.
- S. Chandrasekhar, *Radiative Transfer*, Oxford University Press, London 1960.
- A.D. Klose, A.H. Hielscher, "Quasi-Newton methods in optical tomographic imaging," *Inverse Problems* **19**, 387-409 (2003).
- A.H. Hielscher, A.D. Klose, A.K. Scheel, B. Moa-Anderson, M. Backhaus, U. Netz, and J. Beuthan, "Sagittal laser optical tomography for imaging of rheumatoid finger joints," *Phys. Med. Biol.* **49(7)**, pp. 1147-1163 (2004).
- A.K. Scheel, M. Backhaus, A.D. Klose, B. Moa-Anderson, U. Netz, K. G. Hermann, J. Beuthan, G.A. Muller, G.R. Burmester, A.H. Hielscher, "Comparison of sagittal laser optical tomography with ultrasound and clinical examination for diagnosis of synovitis in PIP joints," *Annals of the Rheumatic Diseases* **64**, pp. 239-245 (2005).
- J. Masciotti, G. Abdoulaev, J. Hur, J. Papa, J. Bae, J. Huang, D. Yamashiro, J. Kandel, A.H. Hielscher, "Combined optical tomographic and magnetic resonance imaging of tumor bearing mice," in: *Optical Tomography and Spectroscopy of Tissue VII*, B.Chance, R.R. Alfano, B.J. Tromberg, M. Tamura, E.M. Sevick-Muraca, eds., SPIE Proc. 5693, pp. 74-81 (2005).

15. J. Masciotti, G. Abdoulaev, F. Provenzano, J. Hur, J. Papa, J. Bae, J. Huang, D. Yamashiro, J. Kandel, A.H. Hielscher, "Optical tomographic and magnetic resonance imaging of tumor growth and regression in mice with VEGF blockade," *27<sup>th</sup> Annual International Conference of the IEEE Engineering in Medicine and Biology Society*, Shanghai (2005).
16. R. Weissleder, U. Mahmood, "Molecular imaging," *Radiology* **219**, pp. 316 (2001).
17. A.D. Klose, V. Ntziachristos, A.H. Hielscher, "In vivo fluorescence molecular imaging with a radiative transfer model," *Molecular Imaging* **3(3)**, p.230 (2004).
18. V. Ntziachristos, C.H. Tung, C. Bremer, R. Weissleder, "Fluorescence molecular tomography resolves protease activity in vivo," *Nature Medicine* **8**, pp. 757(2002).